

Experimental kernel-based quantum machine learning in finite feature space

Karol Bartkiewicz,^{1,2,*} Clemens Gneiting,³ Antonín Černoč,² Kateřina Jiráková,² Karel Lemr,^{2,†} and Franco Nori^{3,4}

¹Faculty of Physics, Adam Mickiewicz University, PL-61-614 Poznań, Poland

²RCPTM, Joint Laboratory of Optics of Palacký University and Institute of Physics of Czech Academy of Sciences, 17. listopadu 12, 771 46 Olomouc, Czech Republic

³Theoretical Quantum Physics Laboratory, RIKEN Cluster for Pioneering Research, 351-0198 Wako-shi, Japan

⁴Department of Physics, The University of Michigan, Ann Arbor, MI 48109-1040, USA

(Dated: December 23, 2021)

We implement an all-optical setup demonstrating kernel-based quantum machine learning for two-dimensional classification problems. In this hybrid approach, kernel evaluations are outsourced to projective measurements on suitably designed quantum states encoding the training data, while the model training is processed on a classical computer. Our two-photon proposal encodes data points in a discrete, eight-dimensional feature Hilbert space. In order to maximize the application range of the deployable kernels, we optimize feature maps towards the resulting kernels' ability to separate points, i.e., their “resolution,” under the constraint of finite, fixed Hilbert space dimension. Implementing these kernels, our setup delivers viable decision boundaries for standard nonlinear supervised classification tasks in feature space. We demonstrate such kernel-based quantum machine learning using specialized multiphoton quantum optical circuits. The deployed kernel exhibits exponentially better scaling in the required number of qubits than a direct generalization of kernels described in the literature.

Introduction. Many contemporary computational problems like drug design, traffic control, logistics, automatic driving, stock market analysis, automatic medical examination, material engineering, and others, routinely require optimization over huge amounts of data [1]. These highly demanding problems can be approached by suitable machine learning (ML) algorithms. However, in many relevant cases the underlying calculations last prohibitively long. These computations could potentially run more efficiently (sometimes exponentially faster) by utilizing quantum resources in ML algorithms (i.e., QML). This speed-up can be partially attributed to the collective processing of quantum information mediated by quantum entanglement. There are various approaches to QML that could be characterized as linear algebra solvers, sampling, quantum optimization, or using quantum circuits as trainable models for inference (see, e.g., Refs. [2–12]). Most of the focus both in classical ML and in QML has been put on deep learning and neural networks. However, recently a promising *kernel-based* approach to supervised QML has been proposed in [10, 11]. It is especially interesting consider its implementation on the platform of linear optics as it does not require quantum memory, but rather combining classical and quantum computations. We theoretically elaborate this kernel-based QML (KQML) for multiphoton quantum optical circuits using a kernel that exhibits exponentially better scaling in the number of required qubits than a direct generalization of kernels previously discussed in the literature. We implement this scheme in a proof-of-principle experiment.

Let us explain KQML by first recalling some definitions and theorems and then we overview the recently proposed method for finding linear boundaries in feature Hilbert space (FHS) [11]. FHS is defined as a space

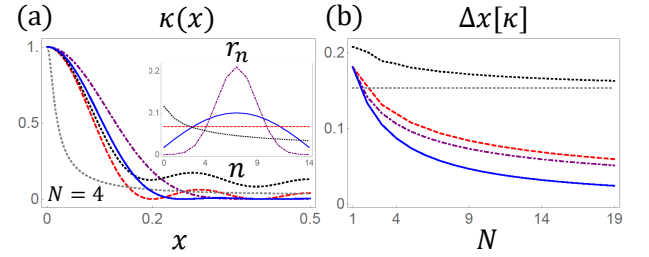


FIG. 1. Kernel family (2) for different amplitude choices. (a) We find that the resolution-optimized kernel (blue solid) exhibits suppressed side maxima as compared to the MSI kernel (red dashed), while the TSQ kernel (with squeezing factor $\zeta = 2$, black dotted) maintains a nonvanishing plateau at all x values. For comparison, we also display the respective squeezed-state kernel for $N \rightarrow \infty$ (gray dotted) and CK (purple dash-dotted). The inset shows the characteristic amplitude progressions for the example $N = 14$ and $\zeta = 4$. (b) The optimized kernel exhibits a significantly improved resolution progression with N as compared to the MSI or the TSQ kernel (here with $\zeta = 3$).

of complex vectors $|\varphi(x)\rangle$, where φ is a feature map (FM) and x is a real vector of dimension D (the input data). FHSs generally have higher dimension than the original data x . This implies that the linear decision boundary in FHS can give rise to a nonlinear decision boundary in the original data space. By virtue of such nonlinear FMs, we do not need to implement nonlinear transformations on the directly encoded data x , which is usually encoded as amplitudes in other QML approaches. Another benefit of KQML is that we can directly measure inner products of vectors mapped onto FHS. Thus, we are able to physically measure a kernel function $\kappa(x', x) = |\langle \varphi(x') | \varphi(x) \rangle|^2$, instead of computing it. This could, in some cases, be much faster than the

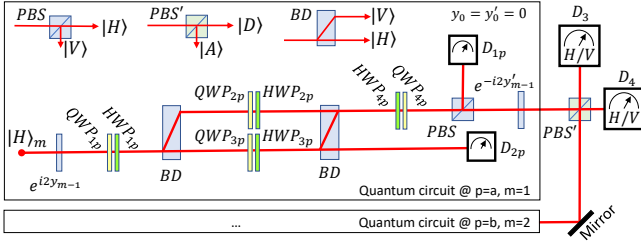


FIG. 2. Optical circuit implementing both the FM and the model circuits. The performance of the setup in QML is shown in Fig. 3 for $N = 1$ and $D = 2$. The experimental setup consists of polarizing beam splitters (PBS s), beam dividers (BD), quarter-wave and half-wave plates ($QWPs$ and $HWPs$, respectively), and single photon detectors D_n for $n = 1a, 1b, 2a, 2b, 3, 4$. D_3 and D_4 are H/V polarization resolving (implemented as a PBS and two standard detectors). The kernel $\kappa(x', x)_{\text{exp}} = [\sum_{p,s=H,V} CC(D_{2s}, D_{3p}) - CC(D_{2V}, D_{3H}) + CC(D_{2H}, D_{3V})] / \sum_{m>n} \sum_{n=1}^6 CC(D_m, D_n)$ is given as a ratio of coincidences $CC(D_m, D_n)$ registered by photon detectors D_n and D_m to the total number of photons.

latter option. It follows from the representer theorem that any function of the reproducing kernel that minimizes the cost function (the solution to the ML problem) can be written as $f^*(x) = \sum_{m=1}^M a_m \kappa(x, x^m)$, where M is the number of training samples, and a_m are some real parameters subject to the training, and x belongs to feature space. Once the kernel κ is known, the parameters a_m can be found very efficiently. The goal of the ML is to find a function $f^*(x)$ that classifies the non-separable points x^1, \dots, x^{M-K} and x^{M-K+1}, \dots, x^M by finding a trade-off between the number of misclassifications and the width of the separating margin. The parameters a_m can be obtained by solving the following problem: minimize $\sum_{m=1}^M (|a_m|^2 + \gamma u_m)$ s.t. $a_i \kappa(x, x^i) \geq 1 - u_i$ for $i = 1, \dots, M - K$ and $a_i \kappa(x, x^i) \leq -(1 - u_i)$ for $i = M - K + 1, \dots, M$, $u \geq 0$, where γ gives the relative weight of the number of misclassified points compared to the width of the margin. In a nutshell, this approach allows to both replace the nonlinearity of the problem with linear multidimensional quantum computations, which offers a potential speed-up.

Kernel resolution in finite dimensions. The ability of a kernel to distinguish data points (i.e., its *resolution*) is an essential hyperparameter, which, for given training data, can decide if a model can be trained successfully or not. If kernel resolution is too coarse, resulting decision boundaries miss relevant details in the data, if it is too refined, the model becomes prone to overfitting. In the infinite-dimensional feature spaces offered by continuous variable implementations, viable FMs with adjustable resolution can be implemented, e.g., by mapping data into squeezed states [11], where the adjustable squeezing factor determines the resolution.

Within the paradigm of discrete, finite-dimensional

quantum information processing, FHS dimension becomes a scarce resource, resulting in limitations on kernel resolution. Let us discuss the optimal kernel resolution that can be achieved in N -dimensional FHS, within the class of FMs of the form

$$x \rightarrow |\psi(x)\rangle = \sum_{n=0}^N \sqrt{r_n} e^{2\pi i n x} |n\rangle, \quad \sum_{n=0}^N r_n = 1, \quad (1)$$

with $\{|n\rangle\}$ a basis of the Hilbert space and $x \in [-1/2, 1/2)$. Any data set can be brought to this form, which is a routine step in data preparation. We stress that the amplitudes r_n are independent from the input values x . The resulting kernels then are of the form

$$\kappa(x, x') = \kappa(x - x') = \left| \sum_{n=0}^N r_n e^{2\pi i n (x' - x)} \right|^2. \quad (2)$$

In this shorthand notation $\kappa(x) \geq 0 \forall x$ and $\kappa(0) = 1$. For the sake of clarity we consider here 1D input data x . For D -dimensional inputs \vec{x} , each input component x_i is encoded separately, requiring an $(N \cdot D + D)$ -dimensional FHS. If the FHS is spanned by q qubits, we have $N = 2^q - 1$. In particular, for $N = 1$ and $r_n = 1/2$ we have $\kappa(x, x') = \cos[\pi(x' - x)]^2$, which realizes a *cosine kernel* (CK). The class of states (1) comprises also truncated squeezed states $|\psi_{\text{TSQ}}(x)\rangle$, with $\sqrt{r_n} = \frac{\sqrt{(2n)!} (-\tanh \zeta)^n}{\sqrt{B} 2^n n! \sqrt{\cosh \zeta}}$ (ζ denotes the squeezing factor and B renormalizes the state after truncation), and, what we call here, *multi-slit interference states* $|\psi_{\text{MSI}}(x)\rangle$, with constant amplitudes $\sqrt{r_n} = 1/\sqrt{N}$. The latter inherit their name from the fact that, by virtue of $\langle x|p\rangle = e^{2\pi i p x}$ ($\hbar=1$), they can be related to a balanced superposition of momentum states in a compact continuous variable Hilbert space (augmented by an internal spin- N degree of freedom), $|\psi_{\text{MSI}}(x)\rangle = \frac{1}{\sqrt{N}} \sum_{n=1}^N \langle x|p=n\rangle |n\rangle$, giving rise to “ N -slit interference” in the position coordinate when projected onto $\langle x| \otimes \frac{1}{\sqrt{N}} \sum_{n=1}^N \langle n|$ [13]. Note that polynomial kernels (discussed, e.g., in [8, 11]) fall outside of the state class (1).

We can use the above compact-space embedding to gain further insight into the nature of our kernel definition (2). If we interpret the states (1) as $|\psi\rangle = \sum_{n=1}^N \sqrt{r_n} |p=n\rangle \otimes |n\rangle$, we can introduce the density operator $\rho = |\psi\rangle\langle\psi|$ and trace over the internal spin degree of freedom, $\rho_{\text{ext}} = \text{Tr}_{\text{int}} \rho = \sum_{n=1}^N r_n |p=n\rangle\langle p=n|$. We then find that the kernel (2) is related to the spatial coherences of the mixed reduced state ρ_{ext} : $\kappa(x, x') = |\langle x|\rho_{\text{ext}}|x'\rangle|^2$.

We define a kernel’s spatial resolution $\Delta x[\kappa]$ by its spatial variance

$$(\Delta x[\kappa])^2 \equiv \int_{-1/2}^{1/2} dx x^2 \tilde{\kappa}(x), \quad (3)$$

where the renormalized kernel $\tilde{\kappa}(x) = \kappa(x)/R$, with $R \equiv \int_{-1/2}^{1/2} dx \kappa(x) = \sum_{n=1}^N r_n^2$, describes a valid probability distribution. In the case of the multi-slit interference states $|\psi_{\text{MSI}}\rangle$, one analytically obtains $(\Delta x[\kappa_{\text{MSI}}])^2 = \frac{1}{12}(1 - S_1(N))$, with the interferometric “squeezing factor” $S_1(N) = -\frac{12}{\pi^2} \sum_{j=1}^{N-1} (-1)^j \frac{N-j}{Nj^2}$, and $N \geq 2$ [13].

The kernel (3) minimizing the resolution is a solution to the optimization problem: minimize $\frac{\vec{r}^T \cdot K \cdot \vec{r}}{|\vec{r}|^2}$ s.t. $\sum_{n=1}^N r_n = 1$, where

$$K_{nm} = \begin{cases} \frac{1}{12}, & n = m \\ \frac{(-1)^{|n-m|}}{2(n-m)^2\pi^2}, & \text{else} \end{cases} \quad (4)$$

and $\vec{r} = (r_1, \dots, r_N)^T$. In Figure 1 we compare this optimized kernel with the TSQ and the MSI kernel. The optimized kernel comes with strongly suppressed side maxima as compared to the MSI kernel, while the TSQ maintains a nonvanishing plateau for all x values. Consequently, the optimized kernel enables, for a given N , a significantly improved resolution as compared to the other kernel choices. The inset of Figure 1a clarifies that amplitudes decaying symmetrically about the “center” state lie at the heart of the performance advantage in terms of kernel resolution.

Although kernels of the form (2) can also be efficiently computed classically, their quantum evaluation may still deliver a significant speed-up. Moreover, seen as a module to be combined with other subroutines, the FMs proposed here may contribute its resource-efficient data point separation ability to an overall setup that comes with an inherently quantum scaling advantage. MSI states, for instance, can be generated in a gate-based quantum computer following the first stage of the phase-estimation algorithm [14].

Cosine kernels. The kernel for our proof of principle demonstration of KQML is defined as $\kappa(x', x) = |\langle \varphi(x') | \varphi(x) \rangle|^2 = \prod_{n=1}^D \cos^{2N}(x'_n - x_n)$, where the FM taking a normalized feature $x_n \in [-\pi/2, \pi/2]$ to FHS is $|\varphi(x)\rangle = \bigotimes_{n=1}^D \sum_{k=0}^N \sqrt{\binom{N}{k}} \sin^k(x_n) \cos^{N-k}(x_n) |k\rangle_n$. Note that N is related to the number of qubits q per dimension as $q = \lceil \log_2(N+1) \rceil$. This FM can also be considered a constant-phase representation of constant-amplitude states. This is the same as representing states either in a basis of eigenstates of x or z components of a collective spin operator. In particular, $(\cos(x)|0\rangle + \sin(x)|1\rangle)/\sqrt{2} \Leftrightarrow (|0'\rangle + e^{2ix}|1'\rangle)/\sqrt{2}$, where $|0\rangle = (|0'\rangle + |1'\rangle)/\sqrt{2}$ and $|1\rangle = (|0'\rangle - |1'\rangle)/\sqrt{2}$.

This mapping uses less resources than the direct product of the map from Ref. [11], i.e., $|\varphi(x)\rangle = \bigotimes_{n=1}^D \bigotimes_{m=1}^N \sum_{k=0}^1 \sin^k(x_n) \cos^{1-k}(x_n) |k\rangle_{n,m}$, where the number of qubits per dimension is $q = N$. Using the powers of CKs allows us to adjust the kernel resolution by choosing the proper value of N . Thus, the number of used qubits can be related directly to the spread of the kernel.

The number of qubits here plays the same role as the squeezing parameter in the experimental proposal given in Ref. [11]. The CK can also include additional $(D-1)$ degrees of freedom by virtue of a FM defined as

$$|\varphi(x)\rangle = \bigotimes_{n=1}^D \sum_{k=0}^N e^{i2y_{n-1}} \sqrt{\binom{N}{k}} \sin^k(x_n) \cos^{N-k}(x_n) |k\rangle_n, \quad (5)$$

where $y_0 = 0$, the number of terms here is $(N+1)^D$, and the associated kernel measured by postselection is $\kappa(x', x) = \prod_{n=1}^D \cos^{2N}(x'_n - x_n) \cos^2(y'_{n-1} - y_{n-1})$.

Optical circuit for KQML. States given by Eq. (5) can be prepared in a quantum optical setup. In the reported proof of principle experiment, we can set $N = 3$ and $D = 2$. This means that, effectively, the experiment deploys $q = 2$ qubits per dimension. The FM is defined via single-photon polarization states (H/V polarization) as well as dual-rail encoding (T/B for top/bottom rail, respectively)

$$|\varphi(x)\rangle = \bigotimes_{n=1}^2 \left(c^3(x_n) |HT\rangle_n + \sqrt{3}s(x_n)c^2(x_n) |HB\rangle_n + \sqrt{3}c(x_n)s^2(x_n) |VB\rangle_n + s^3(x_n) |VT\rangle_n \right), \quad (6)$$

where $c(x_n) \equiv \cos(x_n)$ and $s(x_n) \equiv \sin(x_n)$. This approach is resource-efficient as it only requires two photons to encode x into the FHS state of $N = 3$ and $D = 2$. An optical circuit implementing this FM is depicted in Fig. 2. The top part of the FM circuit works as follows: first, it transforms the standard input $|HB\rangle$ using wave plates resulting in $|HB\rangle \rightarrow (|HB\rangle + |VB\rangle)/\sqrt{2}$. Next, a beam divider separates polarization modes in space, i.e., we have $(|HB\rangle + |VT\rangle)$. Now, the effective operation of wave plates in the top and bottom modes can be described as first transforming $|VT\rangle \rightarrow \mu_T |HT\rangle + \nu_T |VT\rangle$ and $|HB\rangle \rightarrow \mu_B |HB\rangle + \nu_B |VB\rangle$. The parameters are set as $\mu_T = \sqrt{2}c^3(x_n)$, $\nu_T = \sqrt{2}s^3(x_n)$, $\mu_B = \sqrt{6}c^2(x_n)s(x_n)$, $\nu_B = \sqrt{6}c(x_n)s^2(x_n)$. This whole operation is unitary and can be described as $U(x)|HH\rangle = |\varphi(x)\rangle$. The complex conjugate of operation $U(x)$ is $U^\dagger(x')$ and it can be used to express the kernel as $\kappa(x', x) = |\langle HH | U^\dagger(x') U(x) | HH \rangle|^2$. Thus, the circuit $U^\dagger(x')$ for projecting the state $|\varphi(x)\rangle$ to $|\varphi(x')\rangle$ can be constructed as the inverse of the feature embedding $U(x)$ circuit, but for setup parameters set for x' . The next action of the plates in the top and bottom rails is to perform a reverse transformation, but for $x_n = x'_n$. Next, the plates flip the polarizations in the respective rails. Now, the interesting part of the engineered state is in the top rail with flipped polarization. To implement $U(x')^\dagger$, the last pair of waveplates is used both to flip the polarization and to perform the Hadamard transformation. Finally, the *PBS* transmits only H -polarized photons for further processing. The procedure of measuring the kernel $\kappa(x', x)$ can be extended to include additional dimensions, resulting in measuring the kernel

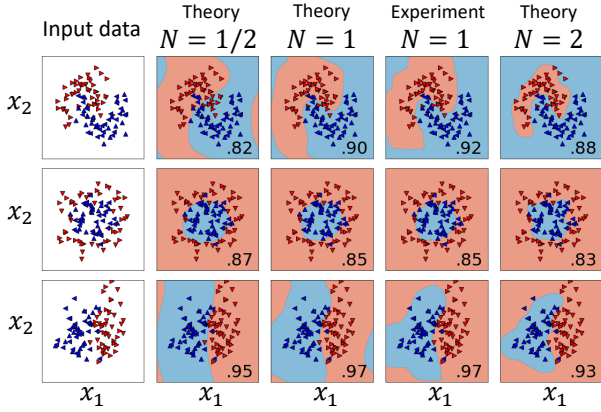


FIG. 3. Training results on a random inseparable data set of 40 samples (up/down-tipped triangles). The performance on a test set (left/right-tipped triangles) of 60 points (the fraction of correctly classified samples that were not used in the QML process) is given in the bottom right corner of each respective subplot. We see that the best choice of CK is $N = 1$. For $N = 2$ we deal with overfitting and for $N = 1/2$ the kernel is too coarse to give as good results as for $N = 1$. The learned classification boundaries are given as contour plots. The slight difference in performance of KQML in relation to the theoretical prediction is due to statistical fluctuations of the experimental data and relatively small test set (misclassification of a single near-boundary point results in 0.02 performance drop).

$\bar{\kappa}(x', x) = \kappa(x', x) \cos^2(y - y')$ following from FM (5). Instead of the transformation $U^\dagger(x')U(x)$, we consider $R^\dagger(y')U^\dagger(x')U(x)R(y)$, where $R(y) = e^{2iy}|H\rangle\langle H|$ is a phase shift applied to a preselected H -polarized photon in the bottom part of the setup, and $R^\dagger(y') = e^{-2iy'}|H\rangle\langle H|$ is a phase shift to the postselected H -polarized photon in the same part of the setup. The phase difference between the postselected upper and lower H -polarized photons can be measured as $\cos^2(y - y')$. This is done with PBS' which transmits diagonally-polarized photons $|D\rangle = (|H\rangle + |V\rangle)/\sqrt{2}$ and reflects antidiagonal photons $|A\rangle = (|H\rangle - |V\rangle)/\sqrt{2}$, and polarization-resolving single-photon detectors (see caption of Fig. 2).

Experimental implementation. We have experimentally implemented KQML to solve three classification problems on a two-photon optical quantum computer. In our experiment we implemented a $D = 2, N = 1$ kernel (using all the modes from Fig. 2, we can set at most $D = 5$ with $q = 1$). We used two photons, but only the top mode of the dual-rail encoding. Including more modes would lead to kernels causing overfitting (see Fig. 3). We have performed measurements for $M = 40$ two-dimensional samples ($D = 2$), drawn from two classes (see horizontally/vertically-tipped triangles in Fig. 3). This procedure was repeated for three benchmark classification problems. For each benchmark $40 \times 39/2 = 780$ measurements were performed to create a corresponding Gramm matrix (GM), which was subsequently used to find the best linear classifi-

cation boundary as given by the representer theorem. In other words, a custom kernel $\kappa(x^m, x^n) = \kappa(x^n, x^m)$ for $m, n = 1, 2, \dots, M$ was measured. This kernel was used as a custom precomputed kernel for the scikit-learn SVC classifier in python. Pairs of H -polarized photons were prepared in a type-I spontaneous parametric down-conversion process in a β -BaB₂O₄ crystal. The crystal was pumped by a 200 mW laser beam at 355 nm (repetition rate of 120 MHz). The coincidence rate, including all possible detection events from Fig. 1, was approximately 250 counts per second. The setup operates with high fidelity (98%) and the dominant source of errors is the Poissonian photon count statistics. We measured each point for a time necessary to collect about 2500 detection events. Thus, excluding the time needed to switch the setup parameters, the whole measurement for a single benchmark problem takes about two hours. To prepare the contour plot of the decision function based on the experimental data shown in Fig. 3 and to quantify the performance of the trained model on the relevant test sets, we have also measured the GM for 1225 points and used its symmetries to fill in the unmeasured values. The values for points in between have been found using linear interpolation. The data accumulation time can be shortened by orders of magnitudes by fine tuning the parameters of the setup and by using brighter photon sources.

Conclusions. We report on the first experimental implementation of supervised QML for solving a nonlinear multidimensional classification problem with clusters of points which are not trivially separated in the feature space. We hope that our research on QML will help to improve ML technologies, which are a major powerhouse of many industries, a vivid field of research in computer science, and an important technique for solving real-world problems. We believe that both the theoretical and the experimental investigation of FM circuits and their constraints regarding kernel resolution and compression for a limited FHS (i.e., FHS size dependent FMs) constitutes a crucial step in the development of practical KQML for SVM QML [8–12]. We demonstrate that a linear-optical setup with discrete photon encoding is a reliable instrument for this class of quantum machine learning tasks. We also report obtaining exponentially better scaling of FHS in the case of CK than in the case of taking direct products of qubits [11]. The same can hold for other more complex kernels implemented in finite FHS, which could appear unfeasible, but in fact require more elaborate FMs (e.g., the resolution-optimized kernels shown in Fig. 1). Thus, KQML can provide a promising perspective for utilizing noisy intermediate-scale quantum systems [15–18], complementing artificial quantum neural networks [19–23] and other hybrid quantum-classical algorithms [24–26].

Acknowledgements Authors acknowledge financial support by the Czech Science Foundation

under the project No. 19-19002S. The authors also acknowledge the projects Nos. LO1305 and CZ.02.1.01./0.0/0.0/16_019/0000754 of the Ministry of Education, Youth and Sports of the Czech Republic financing the infrastructure of their workplace. F.N. is supported in part by the: MURI Center for Dynamic Magneto-Optics via the Air Force Office of Scientific Research (AFOSR) (FA9550-14-1-0040), Army Research Office (ARO) (Grant No. Grant No. W911NF-18-1-0358), Asian Office of Aerospace Research and Development (AOARD) (Grant No. FA2386-18-1-4045), Japan Science and Technology Agency (JST) (via the Q-LEAP program, and the CREST Grant No. JPMJCR1676), Japan Society for the Promotion of Science (JSPS) (JSPS-RFBR Grant No. 17-52-50023, and JSPS-FWO Grant No. VS.059.18N), and the RIKEN-AIST Challenge Research Fund.

* karol.bartkiewicz@upol.cz

† k.lemr@upol.cz

- [1] M. Mohri, A. Rostamizadeh, and A. Talwalkar, *Foundations of Machine Learning* (MIT Press, Cambridge, MA, 2012).
- [2] M. Schuld, I. Sinayskiy, and F. Petruccione, “An introduction to quantum machine learning,” *Contemp. Phys.* **56**, 172 (2015).
- [3] X.-D. Cai, D. Wu, Z.-E. Su, M.-C. Chen, X.-L. Wang, Li Li, N.-L. Liu, C.-Y. Lu, and J.-W. Pan, “Entanglement-based machine learning on a quantum computer,” *Phys. Rev. Lett.* **114**, 110504 (2015).
- [4] J. Biamonte, P. Wittek, N. Pancotti, P. Rebentrost, N. Wiebe, and S. Lloyd, “Quantum machine learning,” *Nature* **549**, 195 (2017).
- [5] M. Schuld, M. Fingerhuth, and F. Petruccione, “Implementing a distance-based classifier with a quantum interference circuit,” *EPL* **119**, 60002 (2017).
- [6] J. Gao, L.-F. Qiao, Z.-Q. Jiao, Y.-C. Ma, C.-Q. Hu, R.-J. Ren, A.-L. Yang, H. Tang, M.-H. Yung, and X.-M. Jin, “Experimental machine learning of quantum states,” *Phys. Rev. Lett.* **120**, 240501 (2018).
- [7] C. Ciliberto, M. Herbster, A. D. Ialongo, M. Pontil, A. Rocchetto, S. Severini, and L. Wossnig, “Quantum machine learning: a classical perspective,” *Proc. R. Soc. A* **474**, 20170551 (2018).
- [8] P. Rebentrost, M. Mohseni, and S. Lloyd, “Quantum support vector machine for big data classification,” *Phys. Rev. Lett.* **113**, 130503 (2014).
- [9] Z. Li, X. Liu, N. Xu, and J. Du, “Experimental realization of a quantum support vector machine,” *Phys. Rev. Lett.* **114**, 140504 (2015).
- [10] R. Chatterjee and T. Yu, “Generalized coherent states, reproducing kernels, and quantum support vector machines,” *Quantum Inf. Commun.* **17**, 1292 (2017).
- [11] M. Schuld and N. Killoran, “Quantum machine learning in feature Hilbert spaces,” *Phys. Rev. Lett.* **122**, 040504 (2019).
- [12] V. Havlíček, A. D. Córcoles, K. Temme, A. W. Harrow, A. Kandala, J. M. Chow, and J. M. Gambetta, “Supervised learning with quantum-enhanced feature spaces,” *Nature* **567**, 209 (2019).
- [13] C. Gneiting and K. Hornberger, “Detecting entanglement in spatial interference,” *Phys. Rev. Lett.* **106**, 210501 (2011).
- [14] M. A. Nielsen and I. Chuang, *Quantum computation and quantum information* (Cambridge University Press, 2002).
- [15] J. Preskill, “Quantum Computing in the NISQ era and beyond,” *Quantum* **2**, 79 (2018).
- [16] K. Fujii and K. Nakajima, “Harnessing disordered-ensemble quantum dynamics for machine learning,” *Phys. Rev. Applied* **8**, 024030 (2017).
- [17] V. Dunjko, Y. Ge, and J. I. Cirac, “Computational speedups using small quantum devices,” *Phys. Rev. Lett.* **121**, 250501 (2018).
- [18] A. Kandala, K. Temme, A. D. Córcoles, A. Mezzacapo, J. M. Chow, and J. M. Gambetta, “Error mitigation extends the computational reach of a noisy quantum processor,” *Nature* **567**, 491 (2019).
- [19] Y. Shen, N. C. Harris, S. Skirlo, M. Prabhu, T. Baehr-Jones, M. Hochberg, X. Sun, S. Zhao, H. Larochelle, D. Englund, *et al.*, “Deep learning with coherent nanophotonic circuits,” *Nat. Photonics* **11**, 441 (2017).
- [20] J. Bueno, S. Maktoobi, L. Froehly, I. Fischer, M. Jacquot, L. Larger, and D. Brunner, “Reinforcement learning in a large-scale photonic recurrent neural network,” *Optica* **5**, 756 (2018).
- [21] F. Tacchino, C. Macchiavello, D. Gerace, and D. Bajoni, “An artificial neuron implemented on an actual quantum processor,” *npj Quantum Information* **5**, 26 (2019).
- [22] S. C. Kak, “Quantum neural computing,” in *Advances in Imaging and Electron Physics*, Vol. 94 (Elsevier, 1995) p. 259.
- [23] E. Farhi and H. Neven, “Classification with quantum neural networks on near term processors (2018),” arXiv:1802.06002.
- [24] Y. Li and S. C. Benjamin, “Efficient variational quantum simulator incorporating active error minimization,” *Phys. Rev. X* **7**, 021050 (2017).
- [25] A. Kandala, A. Mezzacapo, K. Temme, M. Takita, M. Brink, J. M. Chow, and J. M. Gambetta, “Hardware-efficient variational quantum eigensolver for small molecules and quantum magnets,” *Nature* **549**, 242 (2017).
- [26] K. Mitarai, M. Negoro, M. Kitagawa, and K. Fujii, “Quantum circuit learning,” *Phys. Rev. A* **98**, 032309 (2018).